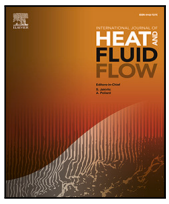
International Journal of Heat and Fluid Flow 122 (2026) 110724



Contents lists available at ScienceDirect

International Journal of Heat and Fluid Flow

journal homepage: www.elsevier.com/locate/ijhff



Multi-objective optimization of bladed cylindrical solar tower receivers using random forest surrogates and NSGA-II

Pedram Alamdari, Mehdi Khatamifar *, Wenxian Lin

College of Science & Engineering, James Cook University, Townsville, QLD 4811, Australia

ARTICLE INFO

Keywords:
Solar towers
Machine learning
Multi-objective optimization
NSGA-II
Random forest
Total heat transfer coefficient
Drag coefficient
Heat-loss

ABSTRACT

Bladed cylindrical receivers have the potential to reduce external heat-losses in solar tower concentrated solar power systems, but their added blades also increase surface area and aerodynamic loading. These competing effects create a coupled thermal–aerodynamic–geometric design problem that has not been fully addressed in previous optimization studies. This work develops a surrogate-assisted multi-objective optimization framework to identify receiver geometries that balance heat-loss reduction, aerodynamic performance, and geometric compactness. Machine-learning surrogate models were trained using a CFD database spanning multiple receiver temperatures, wind conditions, blade lengths, and blade numbers, achieving high predictive accuracy with cross-validated coefficients of determination of about 0.98 for both thermal and aerodynamic responses. The optimization results reveal a consistent trade-off structure across all operating conditions. Very compact designs exhibit both higher drag coefficients and higher total heat-loss coefficients, while highly extended designs reduce the total heat-loss coefficient but introduce excessive surface area and geometric complexity. Between these extremes, a stable intermediate design region provides the best balanced compromise. The surrogate predictions indicate that the knee-point candidates have approximately 43%–52% lower drag coefficients and 33%–40% lower total heat-loss coefficients than the compact design extreme. The proposed framework offers practical design envelopes for early-stage screening of bladed receiver concepts, while indicating that intermediate geometries should be further assessed using high-fidelity simulations before final design selection.

1. Introduction

Fossil fuels still supply a large share of global energy demand and remain a major source of air pollution and greenhouse gas emissions. Expanding low-carbon energy supply is therefore necessary to reduce environmental damage and health impacts. Solar energy is a strong candidate because it is the most abundant energy resource available to Earth (Alamdari et al., 2026b), and its economic competitiveness continues to improve as deployment increases and costs decline (Nijsse et al., 2023).

Solar technologies include several conversion pathways, from direct electricity generation to solar thermal systems. This allows the delivered energy form, either electricity or heat, to be matched more closely to end-use demand (Branz et al., 2015; Madurai Elavarasan et al., 2022). At system scale, electrical or thermal storage and hybrid operation can improve dispatchability, reliability, and capacity utilization (Branz et al., 2015; Alamdari et al., 2024). These features are especially important for industrial applications that require continuous supply or time-shifted heat delivery.

Among solar thermal technologies, concentrated solar power, especially solar tower systems, can deliver high-temperature heat for industrial processes and thermal power generation (Merchán et al., 2022). Solar tower plants still face economic barriers because their capital and maintenance costs are high relative to alternatives such as photovoltaic systems. However, their ability to provide high-temperature heat, dispatchable output through thermal storage, and integration with thermal subsystems continues to motivate work on efficiency improvement and cost reduction. Previous studies have examined heliostat-field design and control (Wang et al., 2019; Besarati et al., 2014), system integration with auxiliary subsystems and storage (Wang et al., 2026; Singh and Narayanan, 2026), and heat-transfer-fluid selection (Yang et al., 2025).

The receiver is a critical component of a solar tower system because it absorbs concentrated solar irradiance and transfers heat to the heat-transfer fluid. Its performance affects thermal efficiency, heat-loss, mechanical loading, and plant cost. Receiver-improvement strategies are commonly divided into internal and external geometric modifications.

* Corresponding author.
E-mail address: mehdi.khatamifar2@jcu.edu.au (M. Khatamifar).

https://doi.org/10.1016/j.ijheatfluidflow.2026.110724
Received 13 May 2026; Received in revised form 22 September 2026; Accepted 23 September 2026
Available online 1 October 2026
0142-727X/© 2026 The Authors. Published by Elsevier Inc. This is an open access article under the CC BY license (http://creativecommons.org/licenses/by/4.0/).

Nomenclature

Greek Symbols

μ_∞	Dynamic viscosity of air at ambient conditions, Pa s
ρ_∞	Density of air at ambient conditions, kg/m^3

Parameters

MARD	Mean absolute relative deviation, %
MRD	Mean relative deviation, %
Re	Reynolds number, $\mathrm{Re} = \rho_\infty U_\infty D_{\mathrm{out}}/\mu_\infty$,
A_{bladed}	External surface area of the bladed receiver, m^2
A_{proj}	Projected area used for drag evaluation, m^2
A_{ratio}	Area ratio, $A_{\mathrm{ratio}} = A_{\mathrm{bladed}}/A_{\mathrm{simple}}$,
A_{simple}	External surface area of the reference simple (Solar Two) receiver, m^2
A_{total}	Total external area used in h_{total}, m^2
C_d	Drag coefficient, $C_d = F_d/(\frac{1}{2}\rho_\infty U_\infty^2 A_{\mathrm{proj}})$,
D_c	Characteristic diagonal length of the receiver core, m
D_{out}	Outer receiver diameter (envelope) used in Re, m
F_d	Aerodynamic drag force, N
h_{conv}	Convective component of the heat-loss coefficient, W/(m^2 K)
h_{rad}	Radiative component of the heat-loss coefficient, W/(m^2 K)
h_{total}	Total (convective+radiative) heat-loss coefficient, $h_{\mathrm{total}} = q_{\mathrm{total}}/[A_{\mathrm{total}}(T_s - T_\infty)]$, W/(m^2 K)
k	Number of folds in k-fold cross-validation,
L_b	Blade length (radial depth), m
L_r	Blade length ratio, $L_r = L_b/D_c$,
N	Number of validation samples (generic index in error metrics),
N_b	Number of blades,
N_{gen}	Number of generations in NSGA-II,
N_{pop}	Population size in NSGA-II,
q_{total}	Total heat-loss (convective+radiative), W
R^2	Coefficient of determination,
T^*	Surface temperature ratio, $T^* = (T_s - T_\infty)/T_\infty$,
T_∞	Ambient (free-stream) temperature, K
T_s	Receiver surface temperature (isothermal boundary condition), K
U_∞	Free-stream wind velocity, m/s

Subscripts

∞	Ambient (free-stream) conditions
bladed	Bladed receiver
conv	Convective
gen	Generation index (NSGA-II)
out	Outer (envelope)
pop	Population (NSGA-II)
proj	Projected
rad	Radiative
ratio	Ratio with respect to simple cylinder
s	Surface (used with temperature: T_s)
simple	Reference simple cylindrical receiver (Solar Two)
total	Combined convective and radiative quantity (used with h and q)

Internal modifications, including buoyant tubes (Rodríguez-Sánchez et al., 2014; Ebadi et al., 2024; Pérez-Álvarez et al., 2025b,a) and finned passages (Shatnawi et al., 2021b,a; Wang et al., 2024; Piña-Ortiz et al., 2019), enhance in-tube heat transfer and reduce wall temperature, but they typically increase pressure drop and geometric complexity. The literature shows that internal strategies improve thermal performance, but their benefit depends on the trade-off among heat-transfer enhancement, pressure drop, stress, and cost. These trade-offs are internal to the tube circuit and do not directly influence the external convective and radiative losses that are the subject of the present study.

External geometric modifications aim primarily to reduce convective and radiative heat-losses and, in some configurations, improve solar interception. Gentile et al. (2025) optimized a star-shaped receiver and reported reductions in both cost and levelized cost of heat relative to a conventional cylindrical receiver. Wang et al. (2020) investigated a bladed cylindrical receiver and reported that a 12-blade configuration reduced total heat-loss relative to a smooth cylinder. (Wang et al., 2022) extended that work to high-temperature operation and reported high receiver efficiency. Wang et al. (2019) showed that blade orientation affects optical efficiency. For billboard geometries, Wang et al. (2023) optimized blade parameters and reported reduced optical and thermal losses. Ghanadi et al. (2020) showed strong sensitivity of convective heat-transfer coefficients to blade length and pitch angle in bladed billboard receivers. Torres et al. (2020) demonstrated that convective and radiative losses respond differently to surface temperature in bladed geometries.

Recent reviews have placed receiver optimization within the broader context of AI-assisted and generative design. Milidonis et al. (2021) reviewed applications of machine learning, evolutionary algorithms, and related AI techniques in solar-tower systems, while Moreno García-Moreno and Milidonis (2025) classified AI-assisted generative-design studies for cavity, external, and volumetric receivers according to approaches including genetic algorithms, particle-swarm optimization, and artificial neural networks.

Taken together, these studies establish that each of the three relevant performance dimensions (thermal loss, aerodynamic loading, and geometric complexity) has been examined in isolation or in pairwise combination for bladed receivers. Thermal loss has been studied against blade geometry (Wang et al., 2020, 2022; Torres et al., 2020); convective coefficients have been related to blade parameters (Ghanadi et al., 2020); and optical-thermal interactions have been analyzed (Wang et al., 2023). However, no study has simultaneously optimized these competing design objectives across a range of wind regimes and temperature conditions for bladed cylindrical receivers.

This gap matters because the relevant thermal, aerodynamic, and geometric effects are coupled in conflicting ways. Adding blades can reduce overall heat-loss through geometric shielding effects, but it also increases the exposed surface area and can change the aerodynamic response depending on blade geometry and flow regime. As a result, optimizing a single objective independently tends to drive the design toward an extreme region of the design space, where improvement in one aspect of performance can be accompanied by penalties in others. A systematic multi-objective approach is therefore necessary to characterize the resulting trade-off surface and identify balanced receiver geometries.

In this study, multi-objective optimization is performed using the authors' previously published numerical database (Alamdari et al., 2026a). The aim is to identify Pareto-optimal geometries for bladed cylindrical receivers across six combinations of wind regime and receiver surface temperature. The objectives are to minimize the total heat-loss coefficient, the drag coefficient, and the receiver area ratio relative to a smooth cylindrical receiver. NSGA-II is an established multi-objective optimization method and has previously been applied to receiver-design problems, including the study by Ma et al. (2025).

The specific contribution of the present study lies in the simultaneous surrogate-assisted optimization of total heat-loss, aerodynamic drag, and receiver area ratio for bladed cylindrical solar-tower receivers across multiple wind and surface-temperature conditions, rather than in the optimization algorithm itself. Because direct CFD evaluation inside

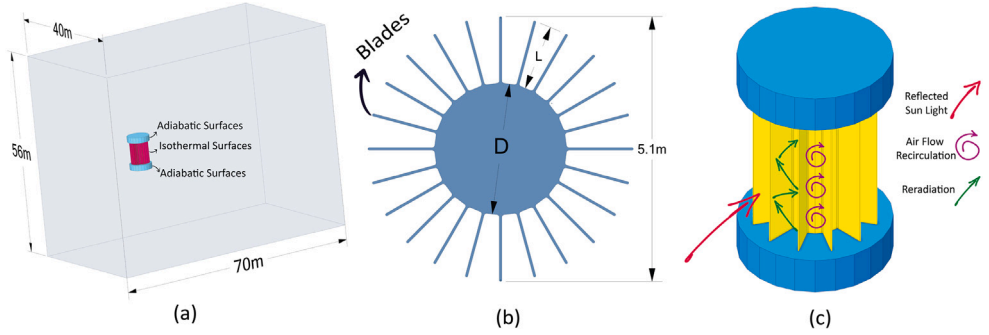


Fig. 1. Computational setup and geometric definition of the bladed cylindrical receiver adopted from the source CFD database. (a) receiver-scale computational domain and thermal boundary conditions; (b) cross-sectional geometric definition; (c) schematic illustration of radiative exchange, reflected sunlight, and airflow recirculation within the bladed receiver.
Source: (a) and (b) are adapted from Alamdari et al. (2026a)

an evolutionary multi-objective optimization loop would require a large number of high-fidelity simulations, random forest surrogate models are developed from the CFD database to provide computationally efficient predictions of the objective functions during NSGA-II optimization. The resulting Pareto fronts are analyzed to identify the dominant trade-offs and to characterize the geometry band that provides the best multi-objective compromise.

2. Methodology

2.1. Data collection

The present optimization uses the complete 216-case CFD database previously published by the authors (Alamdari et al., 2026a); no additional CFD cases were generated for the present study. The source study developed and verified the numerical model and examined the effects of operating conditions and blade geometry on the thermal and aerodynamic responses of the receiver. The present study uses those published response data for a separate decision-oriented analysis comprising random forest surrogate construction and cross-validation, formulation of the three-objective optimization problem, identification of non-dominated design sets, assessment of NSGA-II convergence, and selection of balanced compromise candidates. Fig. 1 summarizes the computational domain and receiver geometry from which the source database was generated.

The dataset was generated using computational fluid dynamics (CFD) simulations of mixed convective and radiative heat transfer from isothermal bladed cylindrical receivers. The simulations covered different surface temperatures, wind speeds, and geometric configurations. The numerical model used the shear-stress transport (SST) k–ω turbulence model, temperature-dependent polynomial air-property correlations, and surface-to-surface radiation modeling. The receiver-scale domain did not extend from the ground; therefore, a local inlet velocity at the receiver elevation was obtained from a power-law atmospheric wind profile and prescribed as the representative approach velocity. Since the receiver height is small compared with the receiver elevation, the mean wind-speed variation over the receiver height is limited, which supports the use of a uniform local inlet velocity in the receiver-scale CFD domain. The source CFD study also included verification against drag-coefficient data and mixed-convection heat-transfer correlations.

The target outputs are the total heat-loss coefficient (h_{total}), the drag coefficient (C_d), and the area ratio (A_{ratio}). The area ratio is defined relative to the surface area of the smooth cylindrical receiver used in the Solar Two project (Pacheco, 2002). As summarized in Table 1, the database covers bladed cylindrical receivers at isothermal surface temperatures of 673.15, 873.15, and 1073.15 K. Six free-stream wind speeds were considered, corresponding to Reynolds numbers from 6.77×10^5 to 4.06×10^6. Three blade-length ratios, $L_r = 0.25, 0.5, 1$, and four blade numbers, $N_b = 4, 8, 12, 24$, were investigated, giving a 3×4 geometric grid. Combined with six Reynolds numbers and three temperatures, the full database comprises 216 CFD cases. In all configurations, blades were attached to the vertices of a central 24-sided polygonal core.

Here, T_s is the isothermal receiver surface temperature and T_∞ is the ambient temperature. The Reynolds number is used as a reference quantity for classifying the imposed wind regime and is defined using the free-stream density ρ_∞, representative receiver-height velocity U_∞, dynamic viscosity μ_∞, and characteristic outer diameter D_{out}. The blade-length ratio is $L_r = L_b/D_c$, where L_b is the blade length and D_c is the characteristic diagonal length of the receiver core. The total heat-loss coefficient is evaluated from the total heat-loss obtained in the CFD solutions as described in Alamdari et al. (2026a). The drag coefficient is based on the drag force F_d and projected area A_{proj}. Finally, $A_{\text{ratio}} = A_{\text{bladed}}/A_{\text{simple}}$, where A_{bladed} is the external surface area of the bladed receiver and A_{simple} is the surface area of the reference Solar Two receiver.

It is important to acknowledge a fundamental characteristic of the source database that shapes all subsequent results. The geometric design space is sampled at only three values of L_r and four values of N_b, producing 12 geometry combinations. This resolution reflects the high computational cost of the underlying CFD simulations and is consistent with the database reported in Alamdari et al. (2026a). Although the random forest models can be evaluated at intermediate L_r values and unsampled integer N_b values within the prescribed bounds, their piecewise-constant predictions do not resolve the physical response continuously between the sampled geometric levels. Any intermediate geometry identified by the optimizer should therefore be interpreted as a surrogate-indicated candidate rather than a directly verified CFD design. This limitation is carried through the analysis and is considered when interpreting the Pareto fronts and knee-point designs.

Blade geometry affects the total heat-loss response, aerodynamic loading, and surface area simultaneously. Surface area is used here as a proxy for manufacturing complexity. The design task is therefore posed as a multi-objective optimization problem in which h_{total}, C_d, and A_{ratio} are minimized with respect to the geometric variables L_r and N_b. Two representative Reynolds numbers, $\text{Re} = 2.03 \times 10^6$ and 4.06×10^6, were selected to represent moderate and high wind regimes. For each wind regime, three temperature ratios were considered, $T^* \in \{1.30, 1.98, 2.66\}$.

2.2. Surrogate modeling of objective functions

Random forest regression was used to construct surrogate models for h_{total}, C_d, and A_{ratio}. The CFD database was treated as supervised learning data, with T^*, Re, L_r, and N_b used as input variables and h_{total},

Table 1
Input and output parameters used for surrogate modeling.

Parameter	Symbol	Definition	Range or values
Input parameters			
Surface-temperature ratio	T^*	$\frac{T_s - T_\infty}{T_\infty}$	1.30 to 2.66
Reynolds number	Re	$\frac{\rho_\infty U_\infty D_{\text{out}}}{\mu_\infty}$	6.77×10^5 to 4.06×10^6
Blade-length ratio	L_r	$\frac{L_b}{D_c}$	0.25, 0.5, 1
Blade number	N_b	Not applicable	4, 8, 12, 24
Output parameters			
Total heat-loss coefficient	h_{total}	$\frac{q_{\text{total}}}{A_{\text{total}}(T_s - T_\infty)}$	15.63 to 98.75 W/(m^2 K)
Drag coefficient	C_d	$\frac{F_d}{\frac{1}{2}\rho_\infty U_\infty^2 A_{\text{proj}}}$	0.96 to 2.86
Area ratio	A_{ratio}	$\frac{A_{\text{bladed}}}{A_{\text{simple}}}$	1.08 to 5.36

C_d, and A_{ratio} used as target outputs. Random forests can represent nonlinear interactions among input variables and are suitable for limited and moderately sized datasets. Bootstrap aggregation and ensemble averaging over finite-depth decision trees reduce variance and mitigate overfitting compared with a single decision tree (Kokol et al., 2022; Xu et al., 2023).

A common hyperparameter set was used for all three surrogate models, as summarized in Table 2. In principle, each objective could benefit from individually tuned hyperparameters, since h_{total} and C_d involve nonlinear aerodynamic and radiative responses while A_{ratio} is a deterministic geometric function. However, with only 216 training samples and a 3 × 4 geometric grid, the number of distinct input combinations is limited, and the risk of overfitting to a specific hyperparameter choice is high. A common, conservatively regularized setting (with a maximum tree depth of 12, a minimum of four samples to split a node, and a minimum of two samples per leaf) was therefore adopted to ensure that all three surrogates are trained under the same generalization constraints. This approach prioritizes reproducibility and cross-objective consistency over marginal accuracy gains that cannot be reliably validated given the available data. The cross-validation results reported in Section 3.1 characterize the predictive performance of this setting for h_{total} and C_d, while the reproduction of the deterministic A_{ratio} relationship is considered separately.

For regression, each tree predicts the mean target value of the samples in the terminal leaf reached by a given input, and the random forest prediction is the average over all trees. This structure is well suited to the present problem because it can represent nonlinear responses and feature interactions without prescribing a functional form (Breiman, 2001).

It should be noted that A_{ratio} is a deterministic function of the geometric inputs L_r and N_b, computed directly from blade and core dimensions. Unlike h_{total} and C_d, which require CFD simulation to evaluate, A_{ratio} carries no stochastic component and can in principle be expressed as a closed-form geometric relation. A random forest surrogate is therefore not required for this quantity in the modeling sense. In the present framework, A_{ratio} is nonetheless included as a surrogate output for implementation consistency, so that all three objectives are evaluated through the same interface during NSGA-II fitness calls. The near-perfect cross-validation accuracy of the A_{ratio} model is a consequence of the underlying geometric identity rather than a modeling achievement, and readers should not conflate it with the predictive performance reported for h_{total} and C_d.

Model performance was assessed using k-fold cross-validation, with 12 folds for h_{total} and C_d, and 6 folds for A_{ratio}. The difference in fold count reflects the dataset structure. The 216 samples for h_{total} and C_d permit 12-fold validation with 18 samples per held-out fold, while the deterministic A_{ratio} model was validated with 6 folds for completeness. Predictive accuracy for h_{total} and C_d was quantified using the coefficient of determination R^2, the mean relative deviation, the mean absolute relative deviation, and the prediction fraction within relative-error thresholds of ±10%, ±20%, and ±30%. The corresponding metrics for A_{ratio} are reported only to document reproduction of the deterministic geometric relationship.

Table 2
Random forest hyperparameters used for all surrogate models.

Hyperparameter	Value
Number of decision trees	1200
Maximum tree depth	12
Maximum features per split	All features (1.0)
Minimum samples to split a node	4
Minimum samples per leaf	2
Bootstrap sampling	Enabled
Out-of-bag scoring	Enabled

$$R^2 = 1 - \frac{\sum_{i=1}^{N}\left(y_i - \hat{y}_i\right)^2}{\sum_{i=1}^{N}\left(y_i - \bar{y}\right)^2}, \tag{1}$$

$$\text{MRD} = \frac{100}{N}\sum_{i=1}^{N}\frac{\hat{y}_i - y_i}{y_i}, \tag{2}$$

$$\text{MARD} = \frac{100}{N}\sum_{i=1}^{N}\left|\frac{\hat{y}_i - y_i}{y_i}\right|, \tag{3}$$

$$\text{PF}(p) = \frac{1}{N}\sum_{i=1}^{N}\mathbb{I}\left(\left|\frac{\hat{y}_i - y_i}{y_i}\right| \le p\right), \tag{4}$$

where y_i and $\hat{y}_i$ are the true and predicted values for sample i, $\bar{y}$ is the validation-set mean, N is the number of validation samples, $\mathbb{I}(\cdot)$ is the indicator function, and $p \in \{0.10, 0.20, 0.30\}$.

2.3. Multi-objective optimization

The non-dominated sorting genetic algorithm II (NSGA-II) was used to approximate Pareto-optimal trade-offs among the three objectives, h_{total}, C_d, and A_{ratio}. The method combines fast non-dominated sorting with a crowding-distance diversity mechanism and can approximate a Pareto front without subjective objective weighting (Deb et al., 2002; Coello Coello, 2006; Konak et al., 2006). It is appropriate here because the objective responses are nonlinear and may be non-convex because of coupled convection, radiation, and separated external flow. The design space is also mixed variable because L_r is treated as continuous and N_b is treated as integer. Reviews of AI-assisted solar-tower and receiver design identify genetic algorithms as an established approach for multi-objective design exploration (Milidonis et al., 2021; Moreno García-Moreno and Milidonis, 2025). Ma et al. (2025) provide a methodological precedent for applying NSGA-II to competing

Table 3
NSGA-II convergence-study protocol.

Item	Setting or definition
Operating conditions	$\mathrm{Re} = 2.03 \times 10^6$ and 4.06×10^6; $T^* = 1.30$, 1.98, and 2.66; six (Re, T^*) combinations
Population sizes tested	100, 200, 500, 1000
Random seeds tested	1 to 5
Generations per convergence run	250
Total convergence runs	$6 \times 4 \times 5 = 120$
Convergence generation	First generation reaching at least 99% of final HV

receiver-performance objectives. The use of NSGA-II with surrogate-model fitness evaluations also follows established surrogate-assisted evolutionary optimization practice for computationally expensive engineering problems (Jin, 2011).

For each operating condition (Re, T^*), the optimization explored the design space defined by L_r and N_b. Six cases were considered from two Reynolds numbers and three temperature-ratio levels. The minimization problem was formulated as

$$\mathbf{f}(L_r, N_b) = \left[h_{\mathrm{total}},\ C_d,\ A_{\mathrm{ratio}}\right]. \tag{5}$$

All fitness evaluations were performed using the surrogate models. The bounds on L_r and N_b were taken from the limits of the training dataset so that the optimization remained within the surrogate domain. As noted in Section 2.1, the source database samples only three blade-length ratios and four blade numbers. Candidate designs at unsampled geometric values should therefore be treated as surrogate-indicated candidates requiring direct CFD verification rather than as validated optima.

As illustrated in Fig. 2, the initial population was generated uniformly within the prescribed bounds. Each candidate was evaluated to obtain h_{total}, C_d, and A_{ratio}. Non-dominated sorting assigned Pareto ranks under minimization, and crowding distance was used to maintain diversity along the trade-off surface. Parent selection followed the standard binary-tournament rule based on lower Pareto rank and, for equal rank, larger crowding distance. Elitism was applied through environmental selection from the combined parent and offspring pool at each generation.

Offspring were generated using crossover and mutation. Crossover recombined design variables from two parent solutions, while mutation introduced small random perturbations to maintain diversity and reduce premature convergence. The integer nature of N_b was enforced by rounding during fitness evaluation and clipping to the admissible bounds when needed, while L_r was treated as continuous.

The optimization loop was repeated for N_{gen} generations. The final non-dominated set returned by NSGA-II was taken as the approximate Pareto front for the corresponding operating condition.

Because each Pareto set contains multiple trade-off solutions, one representative design was selected using a balanced-compromise criterion. For each operating condition, objective values on the Pareto set were linearly scaled to $[0, 1]$. The selected design was the Pareto solution with the minimum Euclidean distance to the ideal point in normalized objective space. The ideal point is the componentwise minimum $\left(\min h_{\mathrm{total}}, \min C_d, \min A_{\mathrm{ratio}}\right)$ over that Pareto set. This normalization treats all three objectives as equally weighted in the compromise metric. Future work could examine whether alternative normalization strategies, such as weighting objectives by their engineering relevance for a given site, would shift the knee location.

2.3.1. NSGA-II convergence

A convergence study was performed to verify that the surrogate-based NSGA-II results are not artifacts of optimizer settings. Hypervolume (HV) was used as the primary convergence indicator. For the present minimization problem, HV measures the normalized objective-space volume dominated by the non-dominated solution set with respect to a prescribed reference point. A larger HV indicates that the Pareto front is closer to the ideal low-objective region or covers a wider portion of the trade-off surface. The protocol and diagnostics are summarized in Table 3.

The convergence study was carried out for all six operating conditions. For each condition, NSGA-II was repeated over four population sizes and five random seeds, giving 120 runs executed for 250 generations each. HV was computed after normalizing all objectives to remove scale-dependent bias. Front diversity and surrogate discretization were assessed using the number of unique non-dominated objective tuples, the non-dominated duplicate ratio, and a spacing metric. CPU time was also recorded. The convergence generation was defined as the first generation at which the HV reached at least 99% of its final value.

Table 4
Random forest training and cross-validation metrics.

Output	Training			Cross-validation		
	R^2	MRD(%)	MARD(%)	R^2	MRD(%)	MARD(%)
h_{total}	0.994	0.3	2.7	0.980	0.4	5.2
C_d	0.993	0.1	1.6	0.981	0.3	2.8
A_{ratio}	1.000	≈ 0	≈ 0	1.000	≈ 0	≈ 0

3. Results and discussion

3.1. Surrogate model accuracy

Table 4 summarizes the training and out-of-fold cross-validation metrics for the random forest representations of h_{total}, C_d, and A_{ratio}. The training results are slightly better than the cross-validation results, as expected. The cross-validated performance remains high for the physically modeled outputs, indicating that the surrogate models capture the main input–output trends without severe loss of generalization.

For h_{total} and C_d, the cross-validated coefficients of determination are $R^2_{\mathrm{CV}} = 0.980$ and 0.981, respectively. The corresponding cross-validated mean absolute relative deviations are approximately 5.2% for h_{total} and 2.8% for C_d. The signed deviations are close to zero, with $\mathrm{MRD}_{\mathrm{CV}} \approx 0.4\%$ for h_{total} and $\approx 0.3\%$ for C_d, indicating that the residuals represent scatter rather than systematic bias. These percentage-based error metrics are rounded to avoid implying a precision smaller than the numerical uncertainty of the CFD database and the additional approximation introduced by the surrogate models. They are therefore used as indicators of surrogate adequacy for trend prediction and Pareto-front screening, rather than as exact measures of physical difference.

As noted in Section 2.2, A_{ratio} is a deterministic geometric function of L_r and N_b. Its near-exact cross-validation accuracy is a consequence of that identity rather than a modeling result. These figures are reported for completeness to confirm that the surrogate correctly recovers the geometric relationship over the sampled database. They carry no implications for prediction accuracy at unseen intermediate geometries.

The prediction-fraction results in Fig. 3 give an interpretable view of the error distribution for the physically modeled outputs. For h_{total}, 90.3% of cross-validated predictions fall within $\pm 10\%$ of the reference values, while all predictions fall within $\pm 20\%$. For C_d, 95.4% of predictions are within $\pm 10\%$, and all predictions fall within $\pm 20\%$. The larger

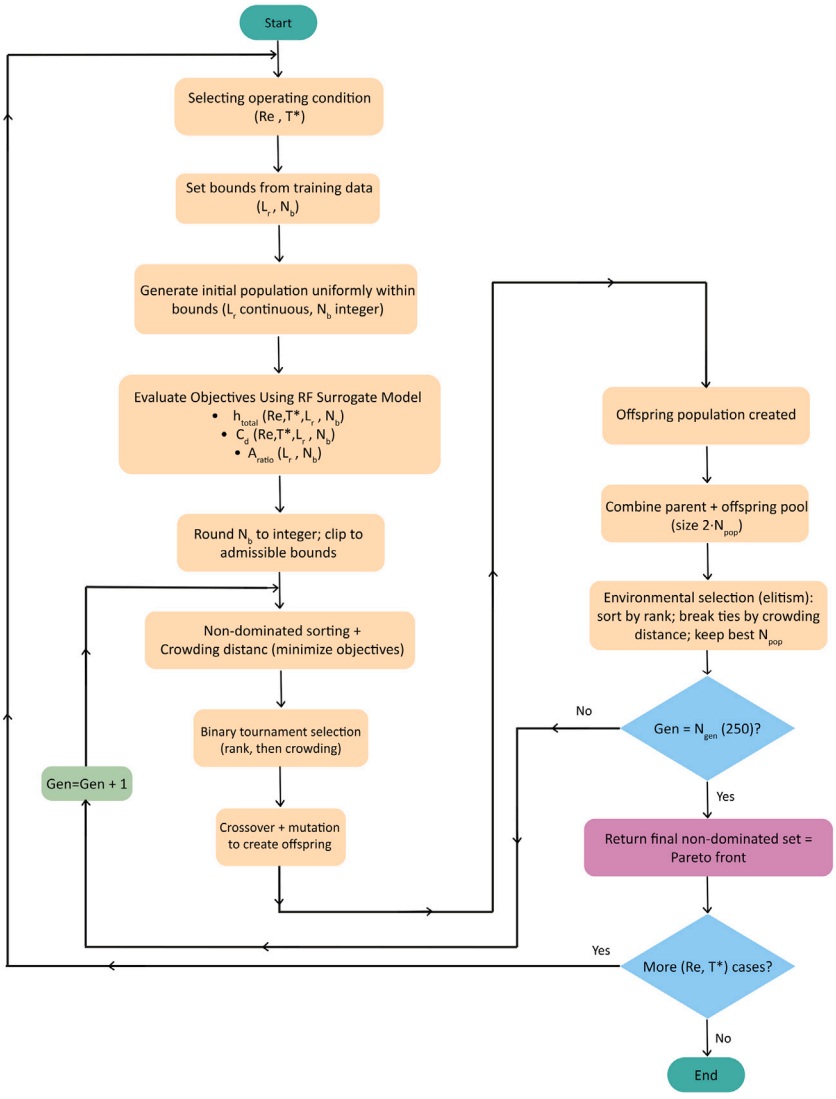


Fig. 2. NSGA-II optimization flowchart.

relative deviations in h_{total} are physically plausible because random forest regression locally averages predictions, which can smooth sharp gradients in regions where the response varies rapidly with geometry or flow condition. In bladed cylindrical receiver flows, separation, reattachment, and near-wall transport can change nonlinearly with Reynolds number, blade length, and blade number. The small signed deviations confirm that this smoothing does not introduce a global directional bias. The surrogate models are therefore suitable for Pareto-front generation and design screening, while final designs should be verified with high-fidelity simulations before treatment as definitive recommendations.

3.2. Kendall rank correlation screening

Fig. 4 shows the Kendall rank correlation map between the operating and design inputs $(T^*, \mathrm{Re}, L_r, N_b)$ and the surrogate outputs $(h_{\text{total}}, C_d, A_{\text{ratio}})$. This analysis is presented as a global screening tool to identify the strongest monotonic associations in the database; it is not a substitute for the random forest's own feature interactions, which capture nonlinear and regime-dependent effects that Kendall τ cannot detect. Weak correlation values should not be interpreted as evidence of physical irrelevance.

The strongest association is between blade number and area ratio, with $\tau \approx 0.87$, which is expected because adding blades directly increases wetted area. Blade length has a weaker positive association with area ratio ($\tau \approx 0.25$), consistent with longer blades increasing surface area less strongly than blade count. For the heat-loss objective, h_{total} correlates positively with T^* ($\tau \approx 0.51$), reflecting stronger radiative emission at higher surface temperature. The negative correlations of h_{total} with N_b and A_{ratio} ($\tau \approx -0.51$ for each) suggest that, globally across the database, geometries with more blades tend to have lower area-normalized heat-loss, consistent with blade self-shielding reducing effective view factors and thus radiative emission per unit area. However, this is a global monotonic trend and does not preclude non-monotonic local behavior at specific Re and T^* combinations.

The drag coefficient C_d has its strongest monotonic association with Reynolds number ($\tau \approx -0.44$), indicating that C_d tends to decrease with increasing Re. For the present sharp-edged bladed geometries, this association should not be read as a migration of the primary separation line. Because the blades are thin radial fins with sharp tips, the dominant separation is geometrically pinned at the blade edges and is essentially Reynolds-number independent, in the same way that separation on a thin flat plate held normal to the flow remains fixed at its edges for any Re (Bearman, 1971). The weak decrease of the normalized C_d with Re instead reflects secondary, Reynolds-number-sensitive effects, namely the transition and reattachment of the shear

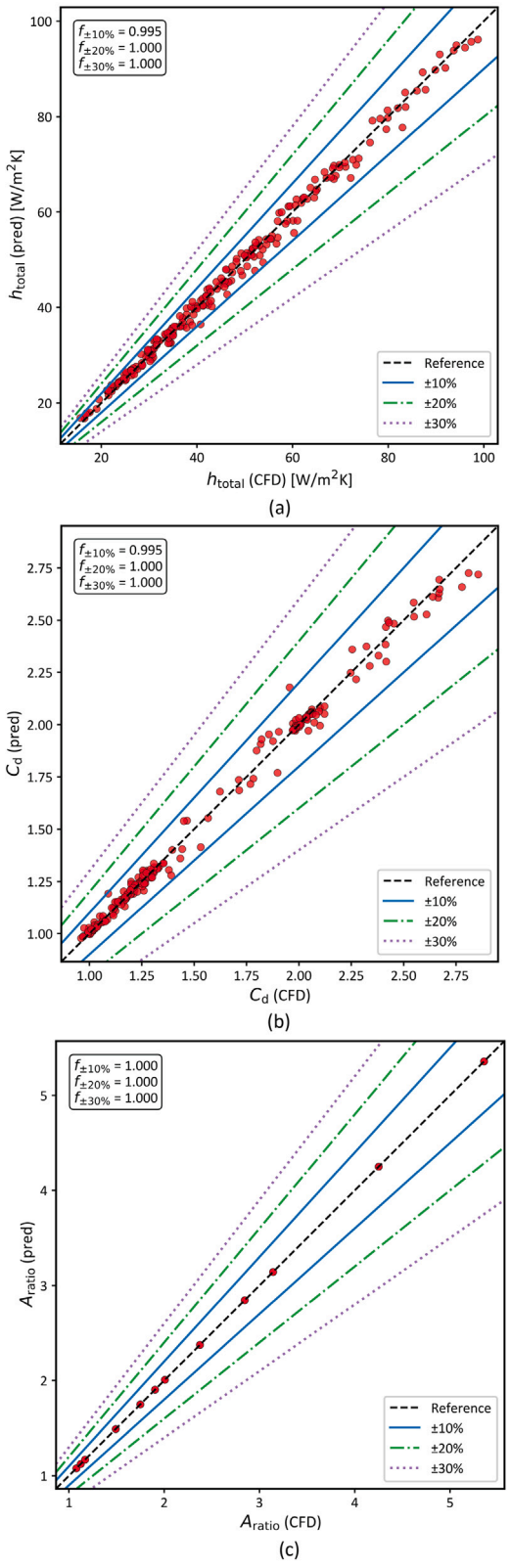


Fig. 3. Prediction-fraction results for h_{total}, C_d, and A_{ratio}.

layers shed from the blade tips and the corresponding recovery of base pressure in the wake, mechanisms that are well documented for cylinders carrying small surface perturbations such as roughness and ribs (Achenbach, 1971; Nakamura and Tomonari, 1982; Skeide et al., 2020). The small magnitude of this effect, well below the drag-crisis variation of a smooth cylinder, is itself consistent with a body whose drag is dominated by sharp-edge separation.

This trend should not be interpreted as a guaranteed reduction in total drag force, since drag force also depends on velocity, density, and reference area. The weaker negative associations of C_d with N_b ($\tau \approx -0.31$) and A_{ratio} ($\tau \approx -0.28$) suggest that more heavily bladed geometries tend to distribute flow disturbance more uniformly, reducing peak momentum deficit in the wake, though this mechanism is geometry- and Re-dependent and is not monotonic across all conditions. All remaining pairwise correlations, including L_r with C_d and Re with A_{ratio}, are near zero.

3.3. NSGA-II optimization

3.3.1. Convergence study

The convergence study was performed over 120 runs spanning the tested population sizes and random seeds. As summarized in Table 5, the 99% HV criterion was reached at Generation 1 in all runs, while the final hypervolume, number of unique non-dominated objective tuples, and spacing metric were identical across the tested settings. These results indicate that the identified Pareto structure is robust to the NSGA-II population sizes and random seeds examined. For this minimization problem, non-dominated (ND) objective tuples are objective vectors for which no other candidate has equal or lower values in all objectives and a lower value in at least one objective; the unique ND count is the number of distinct non-dominated tuples after duplicate objective vectors are removed.

The rapid convergence is consistent with the piecewise-constant structure of the random forest objective functions over the sparsely sampled geometric domain. The initial populations provide broad coverage of the surrogate design space, which explains the early attainment of the final Pareto structure. Importantly, the surrogate-based optimization evaluates intermediate L_r values and admissible integer N_b values within the prescribed bounds, extending the candidate design space beyond the 12 geometric configurations directly evaluated by CFD. The resulting intermediate Pareto and knee-point geometries should therefore be interpreted as surrogate-based design candidates, with targeted high-fidelity CFD verification required before final engineering design selection.

Increasing the population size did not change the final HV, number of unique non-dominated tuples, or spacing metric. It mainly increased the non-dominated duplicate ratio and CPU time. The mean duplicate ratio increased from 0.863 for $N_{pop} = 100$ to 0.986 for $N_{pop} = 1000$, showing that larger populations mostly generated repeated objective tuples. The mean CPU time increased from 144.64 s to 274.47 s. Although $N_{pop} = 100$ recovered the same final Pareto structure, $N_{pop} = 500$ was selected as a conservative production setting. The final optimization runs used $N_{pop} = 500$, $N_{gen} = 10$, and seed = 1.

3.3.2. Pareto front

Fig. 5(a)–(f) presents two-dimensional projections of the three-objective Pareto sets for the six operating conditions. The horizontal axis reports A_{ratio}, the vertical axis reports C_d, and the color of each point represents h_{total}. Each point corresponds to a unique non-dominated receiver geometry after duplicate objective tuples have been removed. The panels are arranged to compare the effect of Reynolds number at fixed temperature ratio. Panels (a) and (d) correspond to $T^* = 1.30$, panels (b) and (e) correspond to $T^* = 1.98$, and panels (c) and (f) correspond to $T^* = 2.66$. Within each fixed-T^* pair, the same h_{total} color scale is used to allow direct comparison between $Re = 2.03 \times 10^6$ and $Re = 4.06 \times 10^6$.

The discrete appearance of the Pareto sets arises from the sparse mixed-variable surrogate landscape rather than from optimizer instability, because N_b is an integer design variable and the random forest

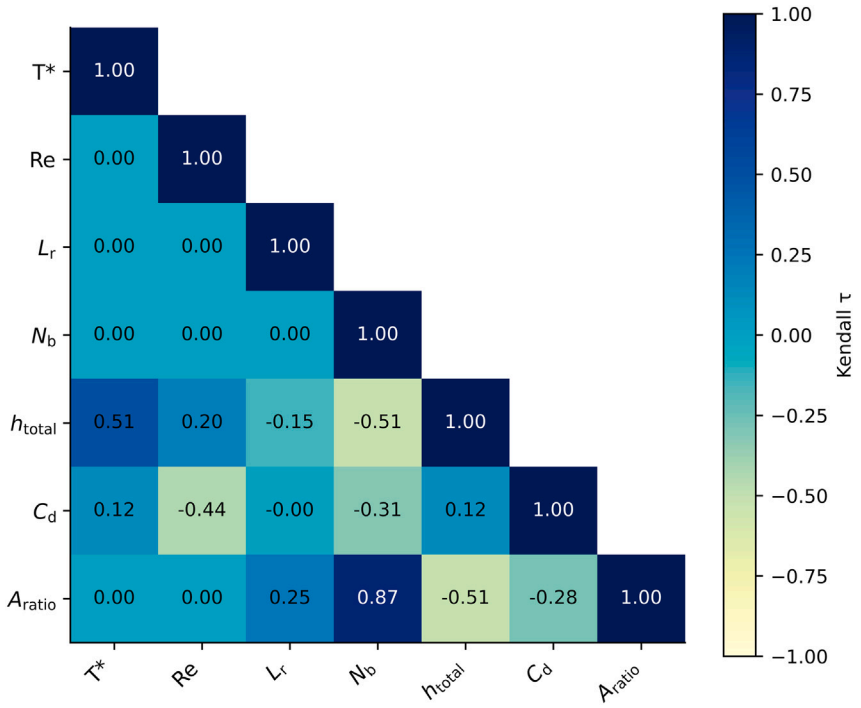


Fig. 4. Kendall rank correlation map for the operating variables, design variables, and surrogate outputs.

Table 5
Summary of NSGA-II convergence behavior using the final common random forest surrogate models.

Condition-wise final convergence metrics					
Re	T^*	Final HV	ND unique	Spacing	Runs
2.03×10^6	1.30	0.729	15	1.304	20
2.03×10^6	1.98	0.736	13	1.080	20
2.03×10^6	2.66	0.725	15	1.127	20
4.06×10^6	1.30	0.759	13	0.905	20
4.06×10^6	1.98	0.764	12	0.816	20
4.06×10^6	2.66	0.753	14	1.162	20
Population-size sensitivity across all conditions and seeds					
N_{pop}	CPU time (s) mean ± std	ND duplicate ratio mean [min, max]	Conv. gen. 99% HV	Exact HV stabilization generation range	
100	144.64 ± 0.57	0.863 [0.850, 0.880]	1	1 to 3	
200	167.67 ± 0.42	0.932 [0.925, 0.940]	1	1 to 3	
500	205.62 ± 0.90	0.973 [0.970, 0.976]	1	1	
1000	274.47 ± 1.97	0.986 [0.985, 0.988]	1	1	

models produce piecewise predictions over the limited CFD training grid.

The plotted Pareto sets identify three distinct design regions. Compact, lightly bladed configurations exhibit relatively high h_{total} and C_d. Their limited blade depth and number provide less mutual radiative shielding, leaving a larger fraction of the receiver surface directly exposed to the colder surroundings. At the same time, the relatively open inter-blade regions permit stronger exchange with the external flow, while exposed blade edges interrupt boundary-layer development and promote separated shear layers and local mixing. These effects are consistent with the larger convective coefficients reported for lightly bladed configurations in the source CFD database (Alamdari et al., 2026a). As blade length and blade number increase, radiative self-shielding becomes stronger and deeper inter-blade regions can restrict ventilation and sustain recirculating flow, reducing the area-normalized thermal-loss coefficient.

The same geometric changes also modify the aerodynamic response by altering pressure-bearing surfaces, shear-layer interactions, and wake development. Consequently, geometries that provide stronger thermal shielding do not necessarily minimize C_d. The intermediate Pareto region represents a balance between these competing mechanisms: it achieves lower predicted thermal loss and drag than the compact configurations without incurring the large surface-area penalty associated with the most extended designs. At the largest $A_{ratio} \approx 5.36$, radiative shielding is strongest and the lowest predicted h_{total} is obtained, but these configurations do not coincide with the minimum-drag solutions. The Pareto structure therefore reflects the competing influence of blade geometry on radiative exposure, convective exchange, aerodynamic loading, and receiver surface area.

These component-level trade-offs complement broader receiver and system-level optimization studies. Gentile et al. (2025) demonstrated the value of considering broader performance and economic criteria when optimizing alternative external-receiver geometries, while Li et al. (2025) considered additional system-level trade-offs associated with tower-integrated cooling. From a methodological perspective, Ma et al. (2025) similarly used NSGA-II to balance competing receiver-performance objectives. Direct numerical comparison with these studies is not attempted because the receiver configurations, operating conditions, and objective definitions differ.

The Reynolds-number effect is most visible in the drag objective. For fixed T^*, increasing Re from 2.03×10^6 to 4.06×10^6 shifts the

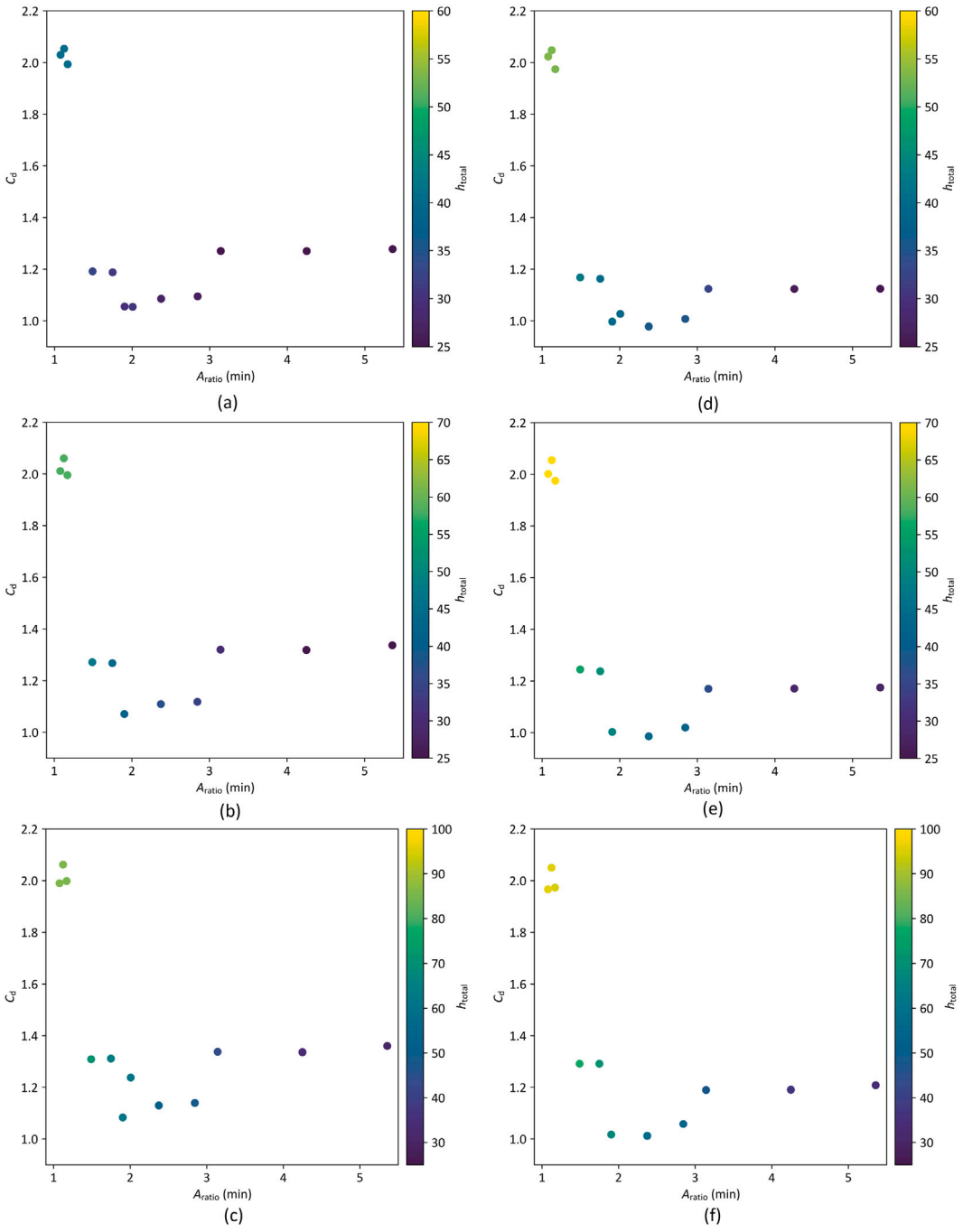


Fig. 5. Pareto fronts for the six operating conditions considered in this study. (a)–(c) correspond to $\mathrm{Re} = 2.03 \times 10^6$ with $T^* = 1.30$, 1.98, and 2.66, respectively. (d)–(f) correspond to $\mathrm{Re} = 4.06 \times 10^6$ with $T^* = 1.30$, 1.98, and 2.66, respectively.

low-drag and intermediate-drag portions of the Pareto set downward. The minimum attainable C_d decreases by about 7% over the paired operating conditions. This residual sensitivity does not arise from a shift in the primary separation line. Because the blades are sharp-edged radial fins, the dominant separation is geometrically pinned at the blade tips and is essentially Reynolds-number independent, as it is for a flat plate held normal to the flow (Bearman, 1971). The small reduction in normalized C_d instead reflects Reynolds-number-sensitive secondary effects, namely the transition and reattachment of the tip shear layers and the associated base-pressure recovery in the wake, which are well documented for cylinders fitted with small surface perturbations and ribs (Achenbach, 1971; Nakamura and Tomonari, 1982; Skeide et al., 2020). Consistent with this, the compact high-drag region remains close to $C_d \approx 2.0$, a value characteristic of a flat-plate-type bluff body rather than a smooth cylinder, so its aerodynamic penalty is governed by geometry-fixed sharp-edge separation rather than by Reynolds-number-dependent separation dynamics. The much smaller Re sensitivity observed here, compared with the drag crisis of a smooth cylinder, is the expected signature of a sharp-edge-dominated geometry.

These observations are consistent with the broader literature on the aerodynamics and heat transfer of cylinders carrying small perturbations. Surface roughness, ribs, and trip elements fix or advance the separation location and shift the cylinder drag crisis to lower Re, so

that the normalized drag of a perturbed cylinder is far less sensitive to Re than that of a smooth one (Achenbach, 1971; Nakamura and Tomonari, 1982; Skeide et al., 2020). The same perturbations that pin separation also enhance convective transport by tripping the boundary layer and promoting separation and reattachment. This is why the source database (Alamdari et al., 2026a) reports the largest convective coefficients for the most lightly bladed configurations, and why experiments on bladed structures report strong convective sensitivity to blade length and pitch (Ghanadi et al., 2020; Torres et al., 2020). In the present Pareto sets, the compact, lightly bladed region therefore corresponds to maximum convective augmentation but minimum radiative self-shielding, which explains why it simultaneously carries high drag and high heat-loss.

The wind approaching a tower receiver is part of the atmospheric boundary layer and can carry high-intensity free-stream turbulence, whereas the source CFD database (Alamdari et al., 2026a) was generated with a uniform velocity inlet at a low prescribed turbulence level. Elevated free-stream turbulence advances shear-layer transition, promotes reattachment, and increases entrainment around bluff bodies (Bearman and Morel, 1983; Norberg and Sundén, 1987), and augments convective heat transfer, particularly in the stagnation and laminar boundary-layer regions of cylinders (Lowery and Vachon, 1975). Two considerations temper the impact of this idealization. First, because separation on the sharp-edged blades is geometrically fixed, the feature that turbulence would otherwise relocate, namely the separation line, is already pinned, so the drag and area-ratio trade-off structure is comparatively robust to the inlet turbulence level. Second, the central results of this study are relative and structural, namely the invariance of the knee geometry band and the separability of the Reynolds-number and temperature effects. Higher free-stream turbulence would raise the absolute convective contribution to h_{total} and shift the thermal-loss level, but is unlikely to overturn the trade-off topology or relocate the knee, which is controlled mainly by area ratio and radiative self-shielding. Extending the database to representative atmospheric turbulence intensities would allow this sensitivity to be quantified directly and is identified as a useful direction for future work.

The heat-loss response depends on both Reynolds number and temperature ratio. At fixed T^*, increasing Re raises the convective contribution to the total heat-loss through stronger external forced convection. At fixed Re, increasing T^* increases the thermal loss level, with a stronger influence on the radiative contribution because radiative heat-loss scales with $T_s^4 - T_\infty^4$. At the highest temperature ratio, the minimum h_{total} changes from approximately 31.1 to 34.1 when Re is doubled, indicating that the thermal response is increasingly controlled by radiation at high receiver temperature. This interpretation is consistent with the CFD trends reported in the source database (Alamdari et al., 2026a). A full quantitative separation of h_{conv} and h_{rad} across the Pareto set is beyond the scope of the present optimization study and is identified as a priority for future work.

A further limitation of the present thermal objective is that h_{total} is an area-normalized combined heat-loss coefficient. Since $q_{\text{total}} = h_{\text{total}} A_{\text{total}}(T_s - T_\infty)$ and A_{total} varies with receiver geometry, a reduction in h_{total} does not necessarily correspond to a proportional reduction in the absolute heat-loss rate. The inclusion of A_{ratio} as a separate optimization objective makes this geometric penalty explicit. In addition, the present isothermal formulation does not resolve local surface-temperature distributions or transient thermo-mechanical response. The dynamic thermal and stress analysis considered by Cui et al. (2025) provides a relevant direction for extending the assessment of the identified candidate geometries toward non-uniform thermal loading and transient operating conditions.

The present optimization is deterministic, with the Pareto fronts obtained for prescribed combinations of Reynolds number and surface temperature. A further extension would therefore be to examine whether the identified intermediate design region remains robust when the operating conditions are uncertain. Luo et al. (2022) demonstrated, at the solar-power-tower system level, that uncertainty propagation can be coupled with multi-objective optimization by considering both the expected performance and its dispersion. A similar robustness framework could be adapted to the present receiver-level problem by assigning appropriate uncertainty distributions to relevant operating parameters and assessing whether the preferred geometry band remains stable under those variations.

Table 6
Knee point geometries selected by the normalized distance criterion and the corresponding predicted objective values.

Re	T^*	L_r	N_b	h_{total}	C_d	A_{ratio}
2.03×10^6	1.30	0.71	13	27.27	1.09	2.37
2.03×10^6	1.98	0.69	11	36.91	1.11	2.37
2.03×10^6	2.66	0.73	15	53.01	1.13	2.37
4.06×10^6	1.30	0.74	12	35.94	0.98	2.37
4.06×10^6	1.98	0.63	12	44.13	0.99	2.37
4.06×10^6	2.66	0.73	16	58.15	1.01	2.37

The influence of T^* appears mainly through h_{total}. At Re = 2.03×10^6, the Pareto-front range of h_{total} increases from approximately 17.7–40.5 at $T^* = 1.30$ to 31.1–85.7 at $T^* = 2.66$. At Re = 4.06×10^6, the corresponding range increases from approximately 25.2–53.4 to 34.1–96.2. By comparison, the area-ratio range is fixed by geometry, and the lowest-drag solutions remain in the intermediate A_{ratio} region. Thus, receiver geometry primarily controls the compactness and drag trade-off, while the operating temperature ratio primarily shifts the thermal loss level on the trade-off surface.

Overall, the Pareto fronts show that the most compact receivers are not preferred because they combine high C_d with high h_{total}. The largest-area solutions provide the lowest h_{total} but require substantially greater receiver surface area and do not provide the lowest C_d.

3.3.3. Knee-point solutions

The non-dominated solutions produced by NSGA-II define a Pareto set for each operating condition. Each design represents a compromise among h_{total}, C_d, and A_{ratio}. Fig. 6(a)–(f) shows these solutions using globally normalized parallel-coordinate plots. Each polyline corresponds to one non-dominated geometry, and the highlighted line denotes the selected knee-point solution. The axes include the three objectives and the corresponding design variables (L_r, N_b).

Across all operating conditions, the parallel-coordinate plots show structured Pareto sets. Compact designs with low A_{ratio} consistently have high normalized C_d and, in several cases, elevated h_{total}, confirming that minimizing area alone leads to simultaneous aerodynamic and thermal penalties. The highlighted knee solutions lie in an intermediate design region with moderate A_{ratio}, low C_d, and intermediate to low h_{total}.

Using the balanced compromise criterion, one representative knee point was selected for each operating condition, as listed in Table 6. The selected geometries fall in a narrow intermediate design band, with $L_r = 0.63$–0.74 and $N_b = 11$–16. All six knee points have the same area ratio, $A_{\text{ratio}} = 2.37$, showing that the normalized distance criterion repeatedly selects the same moderate area region rather than either the compact branch or the highly expanded branch. The corresponding predicted objective values are $C_d = 0.98$–1.13 and $h_{\text{total}} = 27.27$–58.15 W/(m^2 K). These designs should therefore be interpreted as balanced surrogate candidates rather than single objective optima.

To evaluate how the knee point solutions compare with single objective extremes, Table 7 compares the knee point with the minimum h_{total}, minimum C_d, and minimum A_{ratio} reference designs at $T^* = 1.98$. This temperature ratio is used as a representative middle temperature case. The aim of this table is not to repeat every operating condition, but to show how the knee point should be interpreted relative to the three limiting Pareto branches. The same structure is observed at $T^* =$

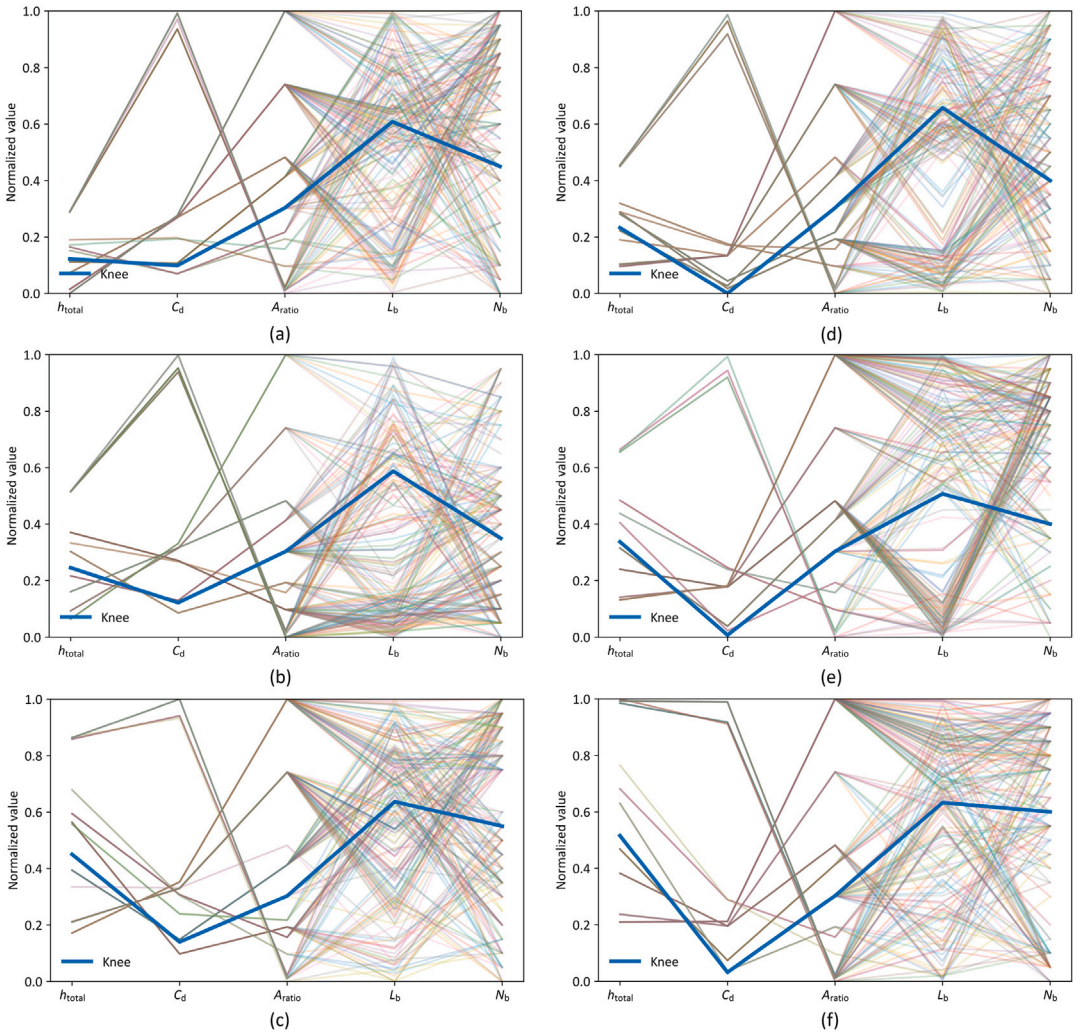


Fig. 6. Parallel-coordinate plots for the six operating conditions considered in this study. (a)–(c) correspond to Re = 2.03×10^6 with $T^* = 1.30$, 1.98, and 2.66, respectively. (d)–(f) correspond to Re = 4.06×10^6 with $T^* = 1.30$, 1.98, and 2.66, respectively.

Table 7
Comparison of Pareto reference designs and knee point solutions at the representative middle temperature ratio $T^* = 1.98$.

Re	Design type	L_r	N_b	h_{total}	C_d	A_{ratio}	h_{knee}/h_{min}	$C_{d,knee}/C_{d,min}$	$A_{ratio,knee}/A_{ratio,min}$
Re = 2.03×10^6, $T^* = 1.98$									
	Knee point	0.69	11	36.91	1.11	2.37	–	–	–
	Min h_{total}	0.97	21	22.65	1.34	5.36	1.63	0.83	0.44
	Min C_d	0.37	15	41.39	1.07	1.90	0.89	1.04	1.25
	Min A_{ratio}	0.31	5	58.20	2.01	1.08	0.63	0.55	2.20
Re = 4.06×10^6, $T^* = 1.98$									
	Knee point	0.63	12	44.13	0.99	2.37	–	–	–
	Min h_{total}	0.95	20	27.94	1.18	5.36	1.58	0.84	0.44
	Min C_d	0.41	18	44.27	0.99	2.37	1.00	1.00	1.00
	Min A_{ratio}	0.26	5	69.87	2.00	1.08	0.63	0.49	2.20

1.30 and $T^* = 2.66$, as shown by the complete reference tables and by Fig. 7. Using the intermediate temperature ratio keeps the table compact while still showing the trade off among heat-loss, drag, and area ratio.

The three ratio columns in Table 7 are calculated by dividing the knee point value by the value of the same objective in the listed reference design. A ratio above one means that the knee point has a larger value for that objective, while a ratio below one means that it has a smaller value. Since all three objectives are minimized, ratios below one indicate an improvement of the knee point relative to that reference design. The ratios should therefore not all be read as penalties.

The complete reference designs for all six operating conditions are given in Tables 8–10. These tables separate the three limiting design choices and make the trade off structure explicit.

The comparison shows that the three extreme branches have very different engineering consequences. The minimum h_{total} designs require the largest geometry in the dataset, with $A_{ratio} = 5.36$ and $N_b = 19$–24. The knee points accept a higher h_{total} than these thermal optima, with $h_{knee}/h_{min} = 1.43$–1.71, but reduce the area ratio by 55.70% and reduce C_d by 13.00%–17.00%. This means that the lowest heat-loss is obtained only by accepting a large increase in receiver area.

Table 8
Reference designs selected by minimum total heat-loss coefficient.

Re	T^*	L_r	N_b	h_{total}	C_d	A_{ratio}
2.03×10^6	1.30	0.82	24	17.65	1.28	5.36
2.03×10^6	1.98	0.97	21	22.65	1.34	5.36
2.03×10^6	2.66	0.76	19	31.14	1.36	5.36
4.06×10^6	1.30	0.98	21	25.15	1.12	5.36
4.06×10^6	1.98	0.95	20	27.94	1.18	5.36
4.06×10^6	2.66	0.80	19	34.10	1.21	5.36

Table 9
Reference designs selected by minimum drag coefficient.

Re	T^*	L_r	N_b	h_{total}	C_d	A_{ratio}
2.03×10^6	1.30	0.99	8	30.55	1.05	2.01
2.03×10^6	1.98	0.37	15	41.39	1.07	1.90
2.03×10^6	2.66	0.34	15	61.90	1.08	1.90
4.06×10^6	1.30	0.74	12	35.94	0.98	2.37
4.06×10^6	1.98	0.41	18	44.27	0.99	2.37
4.06×10^6	2.66	0.41	17	58.19	1.01	2.37

Table 10
Reference designs selected by minimum area ratio.

Re	T^*	L_r	N_b	h_{total}	C_d	A_{ratio}
2.03×10^6	1.30	0.25	6	40.47	2.03	1.08
2.03×10^6	1.98	0.31	5	58.20	2.01	1.08
2.03×10^6	2.66	0.28	6	85.67	1.99	1.08
4.06×10^6	1.30	0.32	4	53.38	2.02	1.08
4.06×10^6	1.98	0.26	5	69.87	2.00	1.08
4.06×10^6	2.66	0.34	6	96.16	1.97	1.08

The minimum C_d designs are closest to the knee points. At Re = 2.03×10^6, the knee points are only 2.90%–4.20% above the minimum drag values, while their h_{total} is 10.70%–14.40% lower than the corresponding minimum drag reference designs. At Re = 4.06×10^6, the knee and minimum drag solutions are effectively identical in C_d. This confirms that the balanced criterion preserves nearly all of the attainable drag reduction.

The minimum A_{ratio} designs form the compact branch. They use few short blades and have $A_{\text{ratio}} = 1.08$, but they also produce the worst aerodynamic and thermal performance, with $C_d \approx 1.97$–2.03 and the highest h_{total} values. The knee points require about 2.20 times the minimum area, but this increase is not wasted area. It gives 43.00%–52.00% lower C_d and 33.00%–40.00% lower h_{total} relative to the compact branch. The knee points are therefore not geometric midpoints. They are intermediate area designs that stay close to the drag optimum while avoiding the high heat-loss of compact receivers and the high area cost of the thermal optimum.

Fig. 7 summarizes the same trade off over all six operating conditions. The drag ratio remains close to unity, with $C_{d,\text{knee}}/C_{d,\text{min}} = 1.00$–1.04, so the knee point retains nearly the full drag benefit of the Pareto set. The heat-loss ratio is higher, with $h_{\text{knee}}/h_{\text{min}} = 1.43$–1.71, because the minimum heat-loss branch requires the largest available area. The area ratio relative to the compact optimum is approximately 2.20 for all conditions. This stable value shows that the balanced solution consistently moves away from the compact branch by the same geometric amount. The result is physically consistent. Very compact receivers reduce surface area, but they also impose large drag and heat-loss penalties. Highly expanded receivers reduce heat-loss, but they do so by using much more area. The knee region is the practical compromise between these two limits.

4. Conclusions

This study developed a surrogate-assisted multi-objective optimization framework for bladed cylindrical solar-tower receiver geometries, simultaneously minimizing total heat-loss coefficient h_{total}, drag coefficient C_d, and area ratio A_{ratio} across six combinations of wind regime and surface temperature. Three broad conclusions emerge from the analysis.

First, the trade-off structure of bladed cylindrical receivers is consistent and predictable across the conditions examined. Compact designs simultaneously exhibit higher drag coefficients and higher total heat-loss coefficients, while large-area designs minimize the total heat-loss coefficient at the expense of geometric complexity and moderate drag. An intermediate region around $A_{\text{ratio}} = 2.374$, $L_r = 0.63$–0.74, and $N_b = 11$–16 provides a stable multi-objective compromise across all six conditions. The fact that the knee-point geometry band is essentially invariant with operating condition suggests that it reflects the fundamental aerodynamic and radiative geometry of the receiver rather than a condition-specific optimum. This is practically useful because the identified intermediate geometry band provides a consistent candidate design family across the wind and temperature conditions examined.

Second, wind speed (Reynolds number) and surface temperature act through physically distinct mechanisms. Increasing Re produces only a modest reduction of the drag coefficient in the intermediate- and low-drag portions of the Pareto front. Because the blades are sharp-edged, the primary separation is pinned at the blade tips and is essentially Reynolds-number independent, so this reduction reflects Reynolds-number-sensitive shear-layer and wake effects rather than a migration of the separation line, and the compact high-drag branch is left essentially unchanged. Increasing T^* primarily raises the heat-loss level across the entire Pareto front, driven by the stronger T^4 scaling of radiative emission relative to convective scaling. These two effects are approximately separable, meaning that the geometric trade-off structure can be characterized once and the heat-loss level can be shifted by temperature without altering the drag and area-ratio relationships.

Third, the present framework demonstrates both the value and the limitations of surrogate-assisted optimization using a sparse database. The random forest surrogates achieve strong cross-validated accuracy for the physically modeled objectives ($R^2_{\text{CV}} = 0.980$ for h_{total} and 0.981 for C_d). Although the underlying database contains only 12 directly simulated geometric combinations, the surrogate-assisted NSGA-II framework enables exploration of intermediate L_r values and admissible integer N_b values within the prescribed design bounds, thereby extending the candidate space beyond the original CFD grid. The convergence analysis shows that the identified Pareto structure is robust across the tested population sizes and random seeds. Nevertheless, geometries identified at unsampled parameter combinations remain surrogate-based candidates and require high-fidelity CFD verification before engineering design selection.

The main limitations are the sparse geometric database, the area-normalized combined heat-loss objective, the low prescribed inlet turbulence, and the omission of optical, internal heat-transfer, and thermo-mechanical effects. Future work should first expand the CFD database around the identified intermediate design region and verify the selected candidates using high-fidelity simulations. Convective and radiative losses should also be evaluated separately, and the influence of representative atmospheric turbulence should be quantified. Future work may also examine the robustness of the identified design region to variations in wind speed and ambient temperature and, following incorporation of optical absorption and receiver energy balance, to variations in solar irradiance. Extending the framework to include optical absorption, internal heat transfer, and receiver energy balance would enable coupling of the present receiver-level optimization with cooling-system and power-cycle models for broader system-level assessment. Finally, transient thermal-stress and control analyses, together with experimental validation, are required to evaluate the identified design candidates under realistic non-uniform and time-dependent operating conditions.

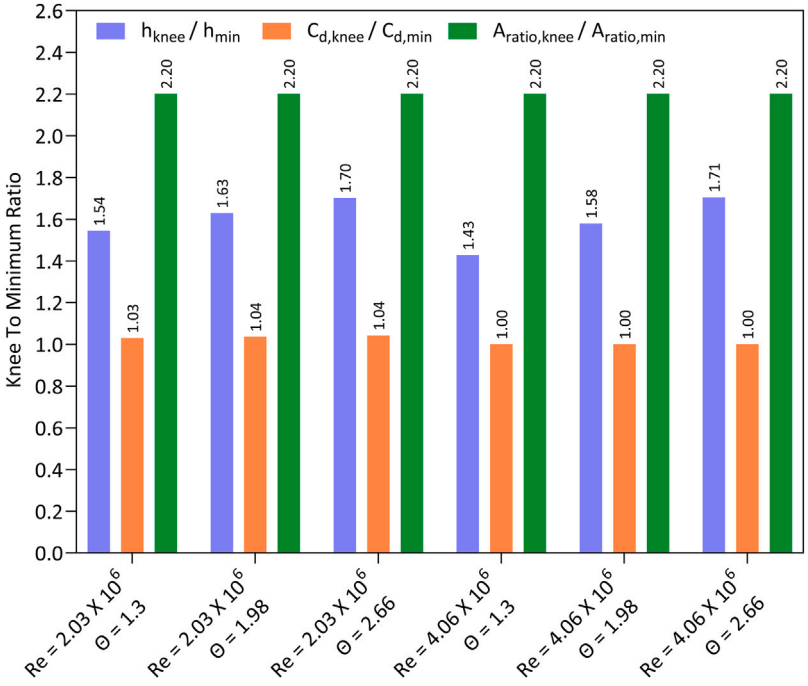


Fig. 7. Ratios of knee point objective values to the corresponding single objective reference values across all six operating conditions.

CRediT authorship contribution statement

Pedram Alamdari: Writing – original draft, Visualization, Methodology, Investigation, Formal analysis, Conceptualization. **Mehdi Khatamifar:** Writing – review & editing, Supervision. **Wenxian Lin:** Writing – review & editing, Supervision.

Declaration of Generative AI and AI-assisted technologies in the writing process

During the preparation of this work, the authors used ChatGPT in order to check grammar and writing style. After using this tool, the authors reviewed and edited the content as needed and take full responsibility for the content of the published article.

Declaration of competing interest

The authors declare that they have no known competing financial interests or personal relationships that could have appeared to influence the work reported in this paper.

Data availability

Data will be made available on request.

References

Achenbach, E., 1971. Influence of surface roughness on the cross-flow around a circular cylinder. J. Fluid Mech. 46 (2), 321–335. http://dx.doi.org/10.1017/S0022112071000569.

Alamdari, P., Khatamifar, M., Lin, W., 2024. Heat loss analysis review: Parabolic trough and linear Fresnel collectors. Renew. Sustain. Energy Rev. 199, 114497. http://dx.doi.org/10.1016/j.rser.2024.114497, URL https://www.sciencedirect.com/science/article/pii/S136403212400220X.

Alamdari, P., Khatamifar, M., Lin, W., 2026a. Mixed convection and radiative heat transfer analysis of a bladed cylindrical receiver. Appl. Therm. Eng. 131335. http://dx.doi.org/10.1016/j.applthermaleng.2026.131335, URL https://www.sciencedirect.com/science/article/pii/S1359431126016431.

Alamdari, P., Khatamifar, M., Lin, W., 2026b. Thermal loss in concentrated solar power plants: A review of external and cavity receivers. Sol. Energy 313, 114585. http://dx.doi.org/10.1016/j.solener.2026.114585, URL https://www.sciencedirect.com/science/article/pii/S0038092X26002732.

Bearman, P.W., 1971. An investigation of the forces on flat plates normal to a turbulent flow. J. Fluid Mech. 46 (1), 177–198.

Bearman, P.W., Morel, T., 1983. Effect of free stream turbulence on the flow around bluff bodies. Prog. Aerosp. Sci. 20 (2), 97–123. http://dx.doi.org/10.1016/0376-0421(83)90002-7, URL https://www.sciencedirect.com/science/article/pii/0376042183900027.

Besarati, S.M., Yogi Goswami, D., Stefanakos, E.K., 2014. Optimal heliostat aiming strategy for uniform distribution of heat flux on the receiver of a solar power tower plant. Energy Convers. Manage. 84, 234–243. http://dx.doi.org/10.1016/j.enconman.2014.04.030, URL https://www.sciencedirect.com/science/article/pii/S0196890414003343.

Branz, H.M., Regan, W., Gerst, K.J., Borak, J.B., Santori, E.A., 2015. Hybrid solar converters for maximum exergy and inexpensive dispatchable electricity. Energy Environ. Sci. 8, 3083–3091. http://dx.doi.org/10.1039/c5ee01998b.

Breiman, L., 2001. Random forests. Mach. Learn. 45 (1), 5–32, http://dx.doi.org/10.1023/A:1010933404324, URL https://doi.org/10.1023/A:1010933404324.

Coello Coello, C., 2006. Evolutionary multi-objective optimization: a historical view of the field. IEEE Comput. Intell. Mag. 1 (1), 28–36. http://dx.doi.org/10.1109/MCI.2006.1597059.

Cui, M., Zhang, Q., Jiang, K., Zheng, M., Niu, Y., Tian, Z., 2025. A multi-objective control strategy for molten salt external receiver in solar tower power plant. Appl. Therm. Eng. 275, 126818. http://dx.doi.org/10.1016/j.applthermaleng.2025.126818, URL https://www.sciencedirect.com/science/article/pii/S1359431125014103.

Deb, K., Pratap, A., Agarwal, S., Meyarivan, T., 2002. A fast and elitist multiobjective genetic algorithm: NSGA-II. IEEE Trans. Evol. Comput. 6 (2), 182–197. http://dx.doi.org/10.1109/4235.996017.

Ebadi, H., Cammi, A., Savoldi, L., 2024. Energetic and exergetic analyses of a double-pass tubular absorber for application in solar towers. J. Sol. Energy Eng. 146 (5), 051013, http://dx.doi.org/10.1115/1.4066201, URL https://doi.org/10.1115/1.4066201, arXiv:https://asmedigitalcollection.asme.org/solarenergyengineering/article-pdf/146/5/051013/7374459/sol_146_5_051013.pdf.

Gentile, G., Carli, F.S., Speranzella, M., Binotti, M., Cholette, M.E., Manzolini, G., 2025. Enhancing solar tower competitiveness with star-shaped receivers. Appl. Energy 391, 125844. http://dx.doi.org/10.1016/j.apenergy.2025.125844, URL https://www.sciencedirect.com/science/article/pii/S0306261925005744.

Ghanadi, F., Torres, J.F., Arjomandi, M., Pye, J., 2020. Flow structure and convective heat transfer in a bladed structure under wind conditions. Int. J. Heat Fluid Flow 85, 108676. http://dx.doi.org/10.1016/j.ijheatfluidflow.2020.108676, URL https://www.sciencedirect.com/science/article/pii/S0142727X20301028.

Jin, Y., 2011. Surrogate-assisted evolutionary computation: Recent advances and future challenges. Swarm Evol. Comput. 1 (2), 61–70. http://dx.doi.org/10.

1016/j.swevo.2011.05.001, URL https://www.sciencedirect.com/science/article/pii/S2210650211000198.
Kokol, P., Kokol, M., Zagoranski, S., 2022. Machine learning on small size samples: A synthetic knowledge synthesis. Sci. Prog. 105 (1), 00368504211029777. http://dx.doi.org/10.1177/00368504211029777.
Konak, A., Coit, D.W., Smith, A.E., 2006. Multi-objective optimization using genetic algorithms: A tutorial. Reliab. Eng. Syst. Saf. 91 (9), 992–1007, Special Issue - Genetic Algorithms and Reliability, https://doi.org/10.1016/j.ress.2005.11.018, URL https://www.sciencedirect.com/science/article/pii/S0951832005002012.
Li, X., Zu, W., Li, Q., Liu, C., Feng, J., 2025. A novel coupled cooling configuration for solar power tower plants: Feasibility analysis and multi-objective optimization. Energy Convers. Manage. 344, 120302. http://dx.doi.org/10.1016/j.enconman.2025.120302, URL https://www.sciencedirect.com/science/article/pii/S019689042500826X.
Lowery, G.W., Vachon, R.I., 1975. The effect of turbulence on heat transfer from heated cylinders. Int. J. Heat Mass Transfer 18 (11), 1229–1242. http://dx.doi.org/10.1016/0017-9310(75)90231-8, URL https://www.sciencedirect.com/science/article/pii/0017931075902318.
Luo, Y., Wang, Z., Zhu, J., Lu, T., Xiao, G., Chu, F., Wang, R., 2022. Multi-objective robust optimization of a solar power tower plant under uncertainty. Energy 238, 121716. http://dx.doi.org/10.1016/j.energy.2021.121716, URL https://www.sciencedirect.com/science/article/pii/S0360544221019642.
Ma, H., Liu, P., Huang, L., Ge, Y., Chen, L., 2025. Performance analysis and heat transfer multi-objective optimization of parabolic trough receiver with annular sector inserts. Sci. China Technol. Sci. 68 (7), 1720101. http://dx.doi.org/10.1007/s11431-024-2807-y, URL https://doi.org/10.1007/s11431-024-2807-y.
Madurai Elavarasan, R., Mudgal, V., Selvamanohar, L., Wang, K., Huang, G., Shafiullah, G., Markides, C.N., Reddy, K., Nadarajah, M., 2022. Pathways toward high-efficiency solar photovoltaic thermal management for electrical, thermal and combined generation applications: A critical review. Energy Convers. Manage. 255, 115278. http://dx.doi.org/10.1016/j.enconman.2022.115278, URL https://www.sciencedirect.com/science/article/pii/S0196890422000747.
Merchán, R., Santos, M., Medina, A., Calvo Hernández, A., 2022. High temperature central tower plants for concentrated solar power: 2021 overview. Renew. Sustain. Energy Rev. 155, 111828. http://dx.doi.org/10.1016/j.rser.2021.111828, URL https://www.sciencedirect.com/science/article/pii/S1364032121010923.
Milidonis, K., Blanco, M.J., Grigoriev, V., Panagiotou, C.F., Bonanos, A.M., Constantinou, M., Pye, J., Asselineau, C.-A., 2021. Review of application of AI techniques to solar tower systems. Sol. Energy 224, 500–515. http://dx.doi.org/10.1016/j.solener.2021.06.009, URL https://www.sciencedirect.com/science/article/pii/S0038092X21004825.
Moreno García-Moreno, J., Milidonis, K., 2025. Generative design of concentrated solar thermal tower receivers—State of the art and trends. Energies 18 (22), http://dx.doi.org/10.3390/en18225890, URL https://www.mdpi.com/1996-1073/18/22/5890.
Nakamura, Y., Tomonari, Y., 1982. The effects of surface roughness on the flow past circular cylinders at high Reynolds numbers. J. Fluid Mech. 123, 363–378. http://dx.doi.org/10.1017/S0022112082003103.
Nijsse, F.J.M.M., Mercure, J.-F., Ameli, N., Larosa, F., Kothari, S., Rickman, J., Vercoulen, P., Pollitt, H., 2023. The momentum of the solar energy transition. Nat. Commun. 14, 6542, Article number 6542, http://dx.doi.org/10.1038/s41467-023-41971-7, URL https://doi.org/10.1038/s41467-023-41971-7.
Norberg, C., Sundén, B., 1987. Turbulence and reynolds number effects on the flow and fluid forces on a single cylinder in cross flow. J. Fluids Struct. 1 (3), 337–357. http://dx.doi.org/10.1016/0889-9746(87)90264-7, URL https://www.sciencedirect.com/science/article/pii/0889974687902647.
Pacheco, J.E., 2002. Final Test and Evaluation Results from the Solar Two Project. Tech. Rep. SAND2002-0120, Sandia National Laboratories, Albuquerque, NM 87185-0703, Editor. Unlimited Release.
Pérez-Álvarez, R., de los Reyes Rodríguez-Sánchez, M., Santana, D., Acosta-Iborra, A., 2025a. Hydraulic-thermal-mechanical optimization of a bayonet tube for solar power tower receivers. Energy 338, 138960. http://dx.doi.org/10.1016/j.energy.2025.138960, URL https://www.sciencedirect.com/science/article/pii/S036054422504602X.
Pérez-Álvarez, R., Marugán-Cruz, C., Santana, D., Acosta-Iborra, A., 2025b. Thermo-hydraulic design and economical manufacturing assessment of bayonet central receivers for solar power towers. Case Stud. Therm. Eng. 75, 107141. http://dx.doi.org/10.1016/j.csite.2025.107141, URL https://www.sciencedirect.com/science/article/pii/S2214157X25014017.
Piña-Ortiz, A., Hinojosa, J., Pérez-Enciso, R., Maytorena, V., Calleja, R., Estrada, C., 2019. Thermal analysis of a finned receiver for a central tower solar system. Renew. Energy 131, 1002–1012. http://dx.doi.org/10.1016/j.renene.2018.07.123, URL https://www.sciencedirect.com/science/article/pii/S0960148118309200.
Rodríguez-Sánchez, M., Sánchez-González, A., Marugán-Cruz, C., Santana, D., 2014. New designs of molten-salt tubular-receiver for solar power tower. Energy Procedia 49, 504–513, Proceedings of the SolarPACES 2013 International Conference, https://doi.org/10.1016/j.egypro.2014.03.054, URL https://www.sciencedirect.com/science/article/pii/S1876610214005086.
Shatnawi, H., Lim, C.W., Ismail, F.B., Aldossary, A., 2021a. An optimisation study of a solar tower receiver: the influence of geometry and material, heat flux, and heat transfer fluid on thermal and mechanical performance. Heliyon 7 (7), e07489. http://dx.doi.org/10.1016/j.heliyon.2021.e07489, URL https://www.sciencedirect.com/science/article/pii/S2405844021015929.
Shatnawi, H., Wai Lim, C., Ismail, F.B., Aldossary, A., 2021b. Experimental study of heat transfer enhancement in solar tower receiver using internal fins. Comput. Mater. Contin. 68 (2), 1693–1711. http://dx.doi.org/10.32604/cmc.2021.016741, URL https://www.sciencedirect.com/science/article/pii/S1546221821010286.
Singh, R., Narayanan, R., 2026. Performance simulation and techno-economic assessment of a concentrated solar thermal power tower plant with thermal storage: A case study of Queensland, Australia. Case Stud. Therm. Eng. 77, 107488. http://dx.doi.org/10.1016/j.csite.2025.107488, URL https://www.sciencedirect.com/science/article/pii/S2214157X25017484.
Skeide, A.K., Bardal, L.M., Oggiano, L., Hearst, R.J., 2020. The significant impact of ribs and small-scale roughness on cylinder drag crisis. J. Wind Eng. Ind. Aerodyn. 202, 104192. http://dx.doi.org/10.1016/j.jweia.2020.104192, URL https://www.sciencedirect.com/science/article/pii/S0167610520301021.
Torres, J.F., Ghanadi, F., Wang, Y., Arjomandi, M., Pye, J., 2020. Mixed convection and radiation from an isothermal bladed structure. Int. J. Heat Mass Transfer 147, 118906. http://dx.doi.org/10.1016/j.ijheatmasstransfer.2019.118906, URL https://www.sciencedirect.com/science/article/pii/S001793101835628X.
Wang, G., Bai, T., Zou, T., Chen, Z., 2026. Comparative study of different schemes of a novel solar tower receiver multigeneration system with SCO2 Brayton cycle and ORC. Renew. Energy 261, 125308. http://dx.doi.org/10.1016/j.renene.2026.125308, URL https://www.sciencedirect.com/science/article/pii/S0960148126001333.
Wang, W.-Q., He, Y.-L., Jiang, R., 2022. A multi-scale solar receiver with peak receiver efficiency over 90% at 720 °C for the next-generation solar power tower. Renew. Energy 200, 714–723. http://dx.doi.org/10.1016/j.renene.2022.09.122, URL https://www.sciencedirect.com/science/article/pii/S0960148122014811.
Wang, K., Liu, Y.-J., Zhang, Z.-D., Zhang, X., Fan, Y.-H., Min, C.-H., 2024. Three-dimensional shape optimization of fins for application in compact supercritical CO2 solar receivers. Int. J. Heat Mass Transfer 221, 125013. http://dx.doi.org/10.1016/j.ijheatmasstransfer.2023.125013, URL https://www.sciencedirect.com/science/article/pii/S0017931023011584.
Wang, W.-Q., Qiu, Y., Li, M.-J., Cao, F., Liu, Z.-B., 2019. Optical efficiency improvement of solar power tower by employing and optimizing novel fin-like receivers. Energy Convers. Manage. 184, 219–234. http://dx.doi.org/10.1016/j.enconman.2018.12.029, URL https://www.sciencedirect.com/science/article/pii/S0196890418313633.
Wang, W.-Q., Qiu, Y., Li, M.-J., He, Y.-L., Cheng, Z.-D., 2020. Coupled optical and thermal performance of a fin-like molten salt receiver for the next-generation solar power tower. Appl. Energy 272, 115079. http://dx.doi.org/10.1016/j.apenergy.2020.115079, URL https://www.sciencedirect.com/science/article/pii/S0306261920305912.
Wang, Y., Zheng, M., Torres, J.F., Shirazi, A., Coventry, J., Pye, J., 2023. Integrated optical–thermal modelling and techno-economic evaluation of a 'bladed' solar-thermal receiver. Sol. Energy 266, 112027. http://dx.doi.org/10.1016/j.solener.2023.112027, URL https://www.sciencedirect.com/science/article/pii/S0038092X23006618.
Xu, P., Ji, X., Li, M., Lu, W., 2023. Small data machine learning in materials science. NPJ Comput. Mater. 9, 42, http://dx.doi.org/10.1038/s41524-023-01000-z, URL https://doi.org/10.1038/s41524-023-01000-z.
Yang, S.-Y., Zhang, J.-Q., Cheng, Z.-D., Jiang, R., He, Y.-L., 2025. Study on a novel dual heat transfer fluid central receiver based on two-level division of non-uniform solar flux. Appl. Therm. Eng. 270, 126250. http://dx.doi.org/10.1016/j.applthermaleng.2025.126250, URL https://www.sciencedirect.com/science/article/pii/S1359431125008427.